Low-Rank Representation-Based Image Super-Resolution Reconstruction with Edge-Preserving

Rui Gao[1,2], Deqiang Cheng[1,*], Jie Yao[1] and Liangliang Chen[1]
[1] School of Information and Control Engineering, China University of Mining and Technology
Xuzhou, Jiangsu 221116 – China
[e-mail:chengdq@cumt.edu.cn]
[2] School of Mathematics and Statistics, Shangqiu Normal University
Shangqiu, Henan 476000 - China
[e-mail: gaorui@cumt.edu.cn]
*Corresponding author: Deqiang Cheng

Received October 6, 2019; revised February 11, 2020; accepted August 24, 2020; published September 30, 2020

Abstract

Low-rank representation methods already achieve many applications in the image reconstruction. However, for high-gradient image patches with rich texture details and strong edge information, it is difficult to find sufficient similar patches. Existing low-rank representation methods usually destroy image critical details and fail to preserve edge structure. In order to promote the performance, a new representation-based image super-resolution reconstruction method is proposed, which combines gradient domain guided image filter with the structure-constrained low-rank representation so as to enhance image details as well as reveal the intrinsic structure of an input image. Firstly, we extract the gradient domain guided filter of each atom in high resolution dictionary in order to acquire high-frequency prior information. Secondly, this prior information is taken as a structure constraint and introduced into the low-rank representation framework to develop a new model so as to maintain the edges of reconstructed image. Thirdly, the approximate optimal solution of the model is solved through alternating direction method of multipliers. After that, experiments are performed and results show that the proposed algorithm has higher performances than conventional state-of-the-art algorithms in both quantitative and qualitative aspects.

Keywords: super-resolution, gradient domain guided image filter, low-rank representation, sparse representation

http://doi.org/10.3837/tiis.2020.09.010 **ISSN : 1976-7277**

1. Introduction

The high resolution (HR) images contain more critical information and rich details, which are widely applied in smart phone camera, remote sensing and object detection. However, since the limitation of camera and the influence of external imaging environment, the resulting images may lose some critical details and the image resolution is lower. Single image super-resolution (SISR) methods, as an effective image processing technology, can produce an excellent HR image from an observed low-resolution (LR) image. In recent years, SISR has become an active topic. Many researchers study various reconstruction methods. The existing methods may generally be classified into three types: interpolation-based approaches [1,2], reconstructed-based approaches [3-11], and learning-based approaches [12-20]. From the perspective of the quality and the speed of the reconstructed image, learning-based approaches reveal their prominent advantages in all SR reconstruction methods. Therefore, in this paper, we focus on the learning-based approaches.

Learning-based or example-based SR methods utilize a learned database consisting of LR and HR image patch pairs to derive the mapping between LR and HR feature spaces, estimating the HR image [21]. According to the establishment of mapping relationship, typical example learning-based SR methods mainly include manifold learning-based approaches [14, 22-24], example regression-based approaches [17, 18, 25], deep learning-based approaches [26-28] as well as sparse representation-based approaches [13, 15, 29, 30]. For example, Chang et al. [14] propose the neighbor embedding (NE) algorithm as the representative of the manifold learning-based methods. This algorithm assumes that the local geometry of the nonlinear manifolds formed by LR image patches is similar to that of their HR counterparts. Timofte et al. [17] propose the anchored neighbor regression (ANR) method, and then on this basis, they combine the best qualities of ANR algorithm and simple functions (SF) to obtain the adjusted anchor neighbor regression (A+) algorithm [18]. Dong et al. propose a model named super-resolution deep convolutional neural network (SRCNN) [26] consisted of three convolutional layers, which directly learns an end-to-end mapping between low- and high-resolution images. Assuming that each LR image patch shares the same sparse coefficient as its corresponding HR patch, Yang et al. utilize the sparse coefficient and the trained HR dictionary to generate a HR image [13]. Dong et al. [15] build a novel adaptive sparse domain selection (ASDS) scheme by integrating local autoregressive (AR) and nonlocal self-similarity (NLSS), which performs well on image deblurring and SR reconstruction. In [30], Huang et al. firstly introduce the gradient domain guided filter [31] into the ASDS scheme, and obtain a novel robust image super-resolution method to preserve edges.

Recently, many researchers have shown great interest in the low-rank representation (LRR) and apply it into image SR reconstruction [3], [32-39], data clustering [40-42], and other fields. In [32], Chen et al. introduce the low-rank matrix recovery (LRMR) technique into the neighbor embedding (NE) SR method and obtain excellent results. Zhao et al. [33] investigate the LRR combining the sparsity with the correlation to establish an adaptive sparse coding-based super-resolution (ASCSR) model. In [35], Lu et al. study the locality-constrained low-rank representation (LLR) and apply it into a unified representation-based face SR framework, constructing HR image. Some low-rank based methods may capture the global structure features of an image and exhibit the powerful SR results. However, these methods have disadvantages, such as blurring edge structures and destroying critical details, since there doesn't exist enough similar patches for any exemplar patch [36, 37]. In order to solve these problems, inspired by [30] and [35], we propose a

representation-based image super-resolution method introducing the gradient domain guided image filter into the LRR scheme. The aim is to reveal the essential structure of an image, and simultaneously preserve its edges during the super-resolution reconstruction.

The major contributions of this paper are:

(1) The prior information of the HR dictionary atom is introduced into the low-rank representation scheme via the gradient domain guided image filter, which can full use of the external high-frequency information to enhance image details.

(2) An effective optimization model is established, which combines the global and local structure information to reveal the intrinsic structure of the input image and simultaneously preserve the edges.

(3) The alternating direction method of the multiplier (ADMM) [43] is used to calculate the approximate solution of the proposed optimization problem, so as to get its representation coefficient.

The rest of the paper is organized as follows. In section 2, we summarize related work on the sparse representation and the low-rank representation. In section 3, the proposed model is described and analyzed in detail. Experiments are performed to compare the proposed model with several conventional methods in section 4. Conclusions are given in section 5.

2. Related Work

In this section, we briefly review the related theories for SR problem, including sparse representation in SISR and low-rank representation, which are important to our proposed model.

2.1 Sparse Representation in Single Image Super-Resolution

The degradation process of image observation is expressed as follows

$$\boldsymbol{Y} = SH\boldsymbol{X} + v, \tag{1}$$

where $\boldsymbol{X}$ and $\boldsymbol{Y}$ respectively represent the original HR image and observed LR image. H is the blurring operator, and S is the down-sampling operator, V represents noise, which is defined as additive Gaussian noise. Sparse representation can effectively tackle the above inverse problem.

In [13], Yang et al. firstly propose sparse representation-based SR method, they exploit the joint dictionary training strategy to get the HR dictionary $\boldsymbol{D}_h$ and the LR dictionary $\boldsymbol{D}_l$, thus the two dictionaries share the same sparse representation coefficeient. After that, the sparse representation coefficient vector can be obtained through solving the following optimization problem.

$$\min_{\alpha} \left\| \boldsymbol{D}_l \boldsymbol{\alpha} - \boldsymbol{y} \right\|_2^2 + \lambda \left\| \boldsymbol{\alpha} \right\|_1, \tag{2}$$

where $\boldsymbol{y}$ denotes the patch of LR image $\boldsymbol{Y}$, $\lambda (\lambda > 0)$ is the regularization parameter that balances the sparsity and the error term. Once the solution $\boldsymbol{\alpha}$ of Eq. (2) is obtained, the corresponding HR feature patch $\boldsymbol{x}$ can be recovered as $\boldsymbol{x} = \boldsymbol{D}_h \boldsymbol{\alpha}$.

2.2 Low-Rank Representation

Given an observation matrix $\boldsymbol{A}$, suppose that $\boldsymbol{A}$ is corrupted by errors or noises $\boldsymbol{E}_0$ ($\boldsymbol{A} = \boldsymbol{D} + \boldsymbol{E}_0$). In order to recover the low-rank matrix $\boldsymbol{D}$ from $\boldsymbol{A}$, consider the following regularized rank minimization problem

$$\min_{\boldsymbol{D}} rank(\boldsymbol{D}), s.t.\ \boldsymbol{A} = \boldsymbol{\Phi D}, \tag{3}$$

where $\boldsymbol{\Phi}$ is the dictionary. More generally, replace the rank function with the nuclear norm to generate the following convex optimization expression

$$\min_{\boldsymbol{D}} \left\|\boldsymbol{D}\right\|_*, s.t.\ \boldsymbol{A} = \boldsymbol{\Phi D}, \tag{4}$$

where $\left\|\boldsymbol{D}\right\|_*$ denotes the kernel norm of $\boldsymbol{D}$ that is the sum of all singular values of the matrix $\boldsymbol{D}$.

The low-rank constraint on matrix $\boldsymbol{D}$ may uncover the $\boldsymbol{A}$'s intrinsic subspace structure and accurately cluster its samples. Therefore, in SR reconstruction, the LRR can uncover the global structure of the image. In the next section, the gradient domain guided filter [31] is incorporated into the LRR scheme to improve the quality of the reconstructed image.

3. Proposed Method

In this section, we detail the proposed model. Firstly, the gradient domain guided image filter is extracted from the HR dictionary, and a LRR model with edge-preserving is constructed, which balances the global intrinsic structure and the local detail enhancement. Then, the representation coefficient of the established optimization model is acquired via the alternating direction method of multiplier (ADMM) [43].

3.1 Model of the Proposed Algorithm

Inspired by Trace Lasso [44], Zhao et al.[33] propose an ASCSR algorithm by introducing a low-rank regularization term: $\left\|\boldsymbol{D}_l diag(\boldsymbol{\alpha})\right\|_*$. Their mathematical form may be written as

$$\min_{\boldsymbol{\alpha}} \left\|\boldsymbol{D}_l\boldsymbol{\alpha} - \boldsymbol{y}\right\|_2^2 + \lambda \left\|\boldsymbol{D}_l diag(\boldsymbol{\alpha})\right\|_*. \tag{5}$$

Due to the characteristics $\boldsymbol{\alpha}_2 \le \left\|\boldsymbol{D}_l diag(\boldsymbol{\alpha})\right\|_* \le \boldsymbol{\alpha}_1$, it can well embody the sparsity and the correlation of image patches. Although the ASCSR algorithm may coordinate the relationship between the sparsity and the correlation via the LRR, the traditional LRR methods cluster similar patches into the same subspace on the assumption that the subspaces are independent. That is, the LRR merely captures the global structure of the data, without taking into account the local structure information. Therefore, it is necessary to further explore the underlying local structure of the data.

The LRR-based SR reconstruction methods usually assume that there are sufficient similar patches to ensure their low-rank property. In practice, the assumption may lose critical image details and edge structure during the process of the reconstruction. Consequently, the edge-preserving is important to the SR reconstruction. By adding a constraint term to the objective function, the LRR is expanded to structure-constrained LRR (SC-LRR) [41] to restrict the structure of its solution, improving performances of the disjoint subspace segment.

The gradient domain guided image filter acted as a local filter may better preserve image edges and enhance image details. As a result, we introduce the gradient domain guided image filter as an edge constraint term into the LRR to boost image reconstruction performance. It can be expressed by the following equation

$$\boldsymbol{\alpha} = \arg\min_{\boldsymbol{\alpha}} \left\{ \left\| \boldsymbol{y} - \boldsymbol{D}_l \boldsymbol{\alpha} \right\|_2^2 + \lambda_1 \left\| \boldsymbol{D}_l diag(\boldsymbol{\alpha}) \right\|_* + \lambda_2 \left\| \boldsymbol{E} \otimes \boldsymbol{\alpha} \right\|_2^2 \right\}, \tag{6}$$

where $\boldsymbol{\alpha} \in R^{d \times 1}$ is the low-rank coding vector. $\otimes$ denotes the element-wise multiplication (the Hadamard product). λ_1 and λ_2 are the parameters that control the balance between low-rank and edge-preserving. $\boldsymbol{E} = \left[e_1, e_2, ..., e_d \right]^T$, $e_i = \exp\left(\dfrac{\left\| \boldsymbol{y} - \hat{\boldsymbol{y}}_G^i \right\|_2^2}{\sigma} \right)$ describes edge constrain, σ is a constant used to adjust the speed of weight decay, and $\hat{\boldsymbol{y}}_G^i$ is the gradient domain guided filter of the i-th atom in $\boldsymbol{D}_h$ dictionary, and $\hat{\boldsymbol{y}}_G^i$ is given by the following equation

$$\hat{\boldsymbol{y}}_G^i = \overline{a}_p \boldsymbol{y}_h^i + \overline{b}_p, \tag{7}$$

where $\boldsymbol{y}_h^i$ is the i-th atom of $\boldsymbol{D}_h$ dictionary, $\overline{a}_p = \dfrac{1}{\left| \Omega_{\zeta_1} \right|} \sum_{p' \in \Omega_{\zeta_1}(p)} a_{p'}$ and $\overline{b}_p = \dfrac{1}{\left| \Omega_{\zeta_1} \right|} \sum_{p' \in \Omega_{\zeta_1}(p)} b_{p'}$ are the mean of $a_{p'}$ and $b_{p'}$ [31].

In the optimization model Eq.(6), the rank minimization of matrix $\boldsymbol{D}_l diag(\alpha)$ means that we may select the most accurate dictionary for the reconstructed image patch $\boldsymbol{y}$ to against noise. In [35], it is confirmed that the structure constraint of subspaces is more necessary than the sparsity so as to obtain better prior information from dictionary atom. For the purpose of taking full advantage of the high-frequency prior information in dictionary atom, we preserve edges by minimizing the difference between the gradient domain guided filter of the HR dictionary atom and the LR input image patch. Therefore, we can simultaneously exploit both the global structure information and the local structure information.

3.2 Deduce the Iterative Algorithm by ADMM

Since the proposed model (6) is convex, the iterative algorithm may be derived by ADMM [42, 43] in order to solve the approximate solution. It may be rewritten as

$$\begin{aligned} &\boldsymbol{\alpha} = \arg\min_{\boldsymbol{\alpha}} \left\{ \left\| \boldsymbol{y} - \boldsymbol{D}_l \boldsymbol{\alpha} \right\|_2^2 + \lambda_1 \left\| \boldsymbol{Z} \right\|_* + \lambda_2 \left\| \boldsymbol{E} \otimes \boldsymbol{\alpha} \right\|_2^2 \right\}, \\ &s.t. \boldsymbol{Z} = \boldsymbol{D}_l diag(\boldsymbol{\alpha}). \end{aligned} \tag{8}$$

The augmented Lagrangian function of the above equation can be expressed as

$$\begin{aligned} L(\boldsymbol{Z},\boldsymbol{\alpha},\boldsymbol{C},\mu) &= \|\boldsymbol{y}-\boldsymbol{D}_l\boldsymbol{\alpha}\|_2^2+\lambda_1\|\boldsymbol{Z}\|_*+\lambda_2\|\boldsymbol{E}\otimes\boldsymbol{\alpha}\|_2^2+\langle \boldsymbol{C},\boldsymbol{Z}-\boldsymbol{D}_l diag(\boldsymbol{\alpha})\rangle \\ &\quad+\frac{\mu}{2}\|\boldsymbol{Z}-\boldsymbol{D}_l diag(\boldsymbol{\alpha})\|_F^2 \\ &= \|\boldsymbol{y}-\boldsymbol{D}_l\boldsymbol{\alpha}\|_2^2+\lambda_1\|\boldsymbol{Z}\|_*+\lambda_2\|\boldsymbol{E}\otimes\boldsymbol{\alpha}\|_2^2+\frac{\mu}{2}\left\|\boldsymbol{Z}-\boldsymbol{D}_l diag(\boldsymbol{\alpha})+\frac{\boldsymbol{C}}{\mu}\right\|_F^2, \end{aligned} \tag{9}$$

where λ_1 and λ_2 are the parameters for balancing different regularization terms, $\boldsymbol{C}$ represents the Lagrange multiplier, $\langle\cdot,\cdot\rangle$ represents the inner product, μ is the penalty parameter, and $\|\cdot\|_F$ is the Frobenius norm. Through alternately calculating each variable in Eq. (9) and fixing remainder variables, we can obtain the solution of all variables. The specific steps are as follows.

Firstly, update the low-rank matrix $\boldsymbol{Z}$, $\boldsymbol{\alpha}$ and other variables are fixed. This can be solved by minimizing the following equation

$$\begin{aligned} \boldsymbol{Z}_{k+1} &= \arg\min_{\boldsymbol{Z}}\left\{\lambda_1\|\boldsymbol{Z}\|_*+\frac{\mu_k}{2}\left\|\boldsymbol{Z}-\boldsymbol{D}_l diag(\boldsymbol{\alpha}_k)+\frac{\boldsymbol{C}_k}{\mu_k}\right\|_F^2\right\} \\ &= \Theta_{\frac{\lambda_1}{\mu_k}}\left(\boldsymbol{D}_l diag(\boldsymbol{\alpha}_k)-\frac{\boldsymbol{C}_k}{\mu_k}\right), \end{aligned} \tag{10}$$

where Θ denotes the singular value threshold (SVT) operator acting on matrix. Defining $Udiag\left(\Psi_{\frac{\lambda}{\mu_k}}(\boldsymbol{\sigma})\right)V^T$ as the singular value decomposition (SVD) of $\boldsymbol{D}_l diag(\boldsymbol{\alpha}_k)-\frac{\boldsymbol{C}_k}{\mu_k}$, then we get the following equation

$$\boldsymbol{Z}_{k+1}=\Theta_{\frac{\lambda_1}{\mu_k}}\left(\boldsymbol{D}_l diag(\boldsymbol{\alpha}_k)-\frac{\boldsymbol{C}_k}{\mu_k}\right)=Udiag\left(\Psi_{\frac{\lambda_1}{\mu_k}}(\boldsymbol{\sigma})\right)V^T, \tag{11}$$

where $\Psi_{\frac{\lambda_1}{\mu_k}}$ represents the SVT operator applying to vector $\boldsymbol{\sigma}$.

Secondly, we update $\boldsymbol{\alpha}_{k+1}$ in Eq. (8), and then the derivation is written as follows

$$\begin{aligned} \boldsymbol{\alpha}_{k+1} &= \arg\min_{\boldsymbol{\alpha}}\left\{\|\boldsymbol{y}-\boldsymbol{D}_l\boldsymbol{\alpha}\|_2^2+\lambda_2\|\boldsymbol{E}\otimes\boldsymbol{\alpha}\|_2^2+\frac{\mu_k}{2}\left\|\boldsymbol{Z}_{k+1}-\boldsymbol{D}_l diag(\boldsymbol{\alpha})+\frac{\boldsymbol{C}_k}{\mu_k}\right\|_F^2\right\} \\ &= \boldsymbol{A}\boldsymbol{D}_l^T\boldsymbol{y}+\boldsymbol{A}diag\left(\boldsymbol{D}_l^T\left(\boldsymbol{Z}_{k+1}+\frac{\boldsymbol{C}_k}{\mu_k}\right)\right), \end{aligned} \tag{12}$$

where $\boldsymbol{A}=\left[\boldsymbol{D}_l^T\boldsymbol{D}_l+\lambda_2 diag(\boldsymbol{E})^T diag(\boldsymbol{E})+diag(diag(\boldsymbol{D}_l^T\boldsymbol{D}_l))\right]^{-1}$.

The Lagrange multiplier $\boldsymbol{C}$ and the penalty parameter μ are updated as follows

$$\begin{aligned} \boldsymbol{C}_{k+1} &= \boldsymbol{C}_k + \mu_k \left(\boldsymbol{Z}_{k+1} - \boldsymbol{D}_l diag(\boldsymbol{\alpha}_{k+1}) \right), \\ \mu_{k+1} &= \min\left(\rho\mu_k, \mu_k \right). \end{aligned} \tag{13}$$

The procedure of the approximate solution of optimization problem (6) based on ADMM is summarized in following Algorithm1. With the solution $\boldsymbol{\alpha}$, the HR image patch is reconstructed by $\boldsymbol{x} = \boldsymbol{D}_h \boldsymbol{\alpha}$.

Algorithm 1 An iterative algorithm based on ADMM for solving the optimization problem (6)

Input: Input image $\boldsymbol{y}$ and initial information $\boldsymbol{Z}_0, \boldsymbol{\alpha}_0, \boldsymbol{C}_0, \mu_0$, regularization parameters λ_1 and λ_2, the learned LR and HR dictionary $\boldsymbol{D}_l$ and $\boldsymbol{D}_h$.
While not converge do
Step 1: Update $\boldsymbol{Z}$ according to Eq. (11), while fix other variables;
Step 2: Update $\boldsymbol{\alpha}$ according to Eq. (12), while fix other variables;
Step 3: Update $\boldsymbol{C}$ and μ according to Eq. (13);
End while
Output: the representation coefficient vector $\boldsymbol{\alpha}$.

3.3 Single Image SR via the Proposed Method

In general, for the example-based SR algorithm, we analyze image characteristics in patches. Therefore, given a LR image $\boldsymbol{Y} \in R^{m \times n}$, to generate a HR image $\boldsymbol{X} \in R^{tm \times tn}$ with the scale factor t, we up-sample the image $\boldsymbol{Y}$ with an interpolation operator, extract gradient features, and divide the resulting feature image into a series of overlapped patches $\boldsymbol{y} \in R^{\sqrt{l} \times \sqrt{l}}$. Then, we concatenate each resulting feature patch into a feature vector. To make the equation be simple, they are still expressed as $\boldsymbol{y} \in R^{l \times 1}$.

In the training stage, the method described in [13] is applied to train dictionary. For each LR feature patch $\boldsymbol{y}$, the HR counterpart $\boldsymbol{x}$ is reconstructed by $\boldsymbol{x} = \boldsymbol{D}_h \boldsymbol{\alpha}$, where the sparse coefficient $\boldsymbol{\alpha}$ is achieved by Algorithm 1. Finally, the mean of $\boldsymbol{y}$ is added to $\boldsymbol{x}$, and all resulting HR image patches are combined into a complete image $\boldsymbol{X}_0$. Furthermore, the global reconstruction constraint (1) is enforced on $\boldsymbol{X}_0$ to obtain a more satisfactory reconstructed image, as follows

$$\boldsymbol{X}_* = \arg\min_{\boldsymbol{X}} \left\| \boldsymbol{Y} - \boldsymbol{SHX} \right\|_2^2 + c \left\| \boldsymbol{X} - \boldsymbol{X}_0 \right\|. \tag{14}$$

The Eq. (14) is solved by gradient descent method, and its iterative update is written as follows

$$\boldsymbol{X}_{t+1} = \boldsymbol{X}_t + v\left[H^T S^T (\boldsymbol{Y} - \boldsymbol{SHX}_t) + c(\boldsymbol{X}_t - \boldsymbol{X}_0) \right]. \tag{15}$$

The following Algorithm 2 summarizes how to perform single image super-resolution reconstruction via our proposed approach.

Algorithm 2 SISR via LRR and gradient prior

Input: LR image $\boldsymbol{Y}$, the learned LR dictionary $\boldsymbol{D}_l$ and HR dictionary $\boldsymbol{D}_h$, scale factor t, regularization parameters λ_1 and λ_2.

Step1: Upscale the LR image $\boldsymbol{Y}$ via an interpolation operator with scale factor t, and extract gradient feature of $\boldsymbol{Y}$.

Step2: Divide $\boldsymbol{Y}$ into a series of overlapped patches $\{\boldsymbol{y}_i\}_{i=1}^{b}$.

Step3: For each feature patch $\boldsymbol{y}_i : i = 1 \text{ to } b$.

Step4: For each HR dictionary atom $d_h^j : j = 1 \text{ to } m$.

Step5: Extract the gradient-domain guided filter of d_h^j.

Step6: Calculate its corresponding sparse representation coefficient $\boldsymbol{\alpha}_i$ via our proposed Algorithm 1.

Step7: Compute the corresponding HR feature patch $\boldsymbol{x}_i = \boldsymbol{D}_h \boldsymbol{\alpha}_i$, add the mean of $\boldsymbol{y}_i$, and then generate the HR image patch.

Step8: End for i.

Step9: End for j.

Step10: Stitch all resulting HR image patches to form a whole initial HR image $\boldsymbol{X}_0$.

Step11: Obtain the final HR image under the global reconstruction constraint (14).

Output: The desired HR image.

4. Experiments and Analysis

In this paper, experiments are all implemented on an Intel(R) Core(TM) i7-6500U PC under the Matlab R2017b programming environment. We choose several natural HR images from Set 5, Set 10, Set 14 used in [15] and [18], as shown in **Fig. 1**. To objectively evaluate the performance of reconstructed HR images, the peak signal-to-noise ratio (PSNR) and the structural similarity (SSIM) are acted as experimental evaluation criteria.

In the experiment, the size of the patch is set to 5×5, the overlap between adjacent patches is 1 pixel, and the magnification of the LR image is 2 or 3. For a color image, the human visual system (HVS) is more sensitive to the variation in luminance, so we apply our proposed method to the luminance channel (Y channel in YCbCr color space) and apply the bicubic interpolation to the Cb and Cr channel. All dictionaries are obtained by training 100000+ pairs of patches and their sizes are set to 1024, which is as similar as [13].

Fig. 1. Ten HR test images, from left to right and from top to bottom: Plants, Bike, Butterfly, Flower, Girl, Parthenon, Leaves, Parrots, Raccoon, Starfish.

4.1 Effectiveness of Our Proposed Method

In this subsection, our method is compared with Bicubic interpolation, ScSR [13], ANR [17], ASCSR [33], SRCNN [26], ASR+LR [34], and the experimental results on ten images shown in **Fig. 1** are presented. We set the identical parameter $\lambda_1 = 0.2$ as in the paper [33], and $\lambda_2 = 0.1$. The selection of the parameter λ_2 may be specifically discussed in section 4.2. And the initial values of $\boldsymbol{\alpha}$, $\boldsymbol{Z}$ and $\boldsymbol{C}$ are all set to zero. **Table 1** and **Table 2** respectively list the PSNR and SSIM results obtained by our approach and the abovementioned methods when magnification factors are 2 and 3.

As listed in **Table 1** and **Table 2**, SRCNN shows the best results. In all the sparse representation-based methods, ASR+LR achieves the best results on Flower and Girl images, and the highest SSIM values are also achieved on Plants and Parrots images, which indicates the ASR+LR method can enhance structure information. However, the PSNR and SSIM averages obtained via our reconstruction method are the highest among all the sparse representation-based methods, which fully demonstrates the effectiveness and superiority of our approach.

To visually evaluate the proposed approach, **Fig. 2** shows the visual contrast results with a magnification of 2 on image Leaves, **Fig. 3** and **4** show the visual detail comparison of the Plants and Butterfly images with a magnification of 3. Adding an edge-preserving regularization term, the sharp edges and rich details are well restored. Take **Fig. 3** as an example, we can observe that the Bicubic interpolation generates a bit blur in the reconstructed image Plants, while ScSR and ANR have sharper outline and edges, with some ringing artifacts, ASCSR and ASR+LR have a certain improvement in visual effect. Deep learning-based methods have performed excellently in image SR, but they still have some

disadvantages. For example, they always need large amounts of data for training, which are sometimes difficult to obtain. In addition, they usually take a lot of time even several days to train the network on very sophisticated graphical processing units (GPUs). In this paper, we exploit the method in [13] without requiring a great many of data and spending too much time to build a couple dictionary. To sum up, our jobs not only have higher performance to reveal the details of the image but also have better actual SR reconstruction effect.

Fig. 2. Comparison of SR results on Leaves by different methods (scaling factor $s = 2$), from left to right and from top to bottom: Bicubic, ScSR[13], ANR[17], ASCSR[33], SRCNN[26] , ASR+LR[34], Proposed method.

Table 1. Comparison of our method with Bicubic, ScSR[13], ANR[17], ASCSR[33], SRCNN[26] and ASR+LR[34](scaling factor $s = 2$).

Image		Criterion	Bicubic	ScSR	ANR	ASCSR	SRCNN	ASR+LR	Ours
Plants	×2	PSNR	34.3255	35.7928	35.7582	35.7315	36.7636	35.8236	35.9888
		SSIM	0.9208	0.9332	0.9322	0.9333	0.9401	0.9358	0.9355
Bike	×2	PSNR	25.6630	26.9336	26.9867	27.0023	27.8295	27.2321	27.4201
		SSIM	0.8362	0.8725	0.8730	0.8738	0.8893	0.8797	0.8832
Butterfly	×2	PSNR	27.4643	28.9296	29.0873	29.1028	31.2009	29.1877	29.3427
		SSIM	0.9176	0.9190	0.9207	0.9212	0.9399	0.9243	0.9256
Flower	×2	PSNR	30.4534	31.5976	31.6231	31.8501	32.4880	32.0036	31.9317
		SSIM	0.8823	0.9027	0.9029	0.9032	0.9156	0.9092	0.9083
Girl	×2	PSNR	34.7490	35.0868	35.1954	35.2023	35.6162	35.4112	35.3979
		SSIM	0.7791	0.7993	0.8013	0.8017	0.8064	0.8038	0.8036
Parthenon	×2	PSNR	28.1119	28.6806	28.7564	28.7788	29.4198	28.8144	28.9578
		SSIM	0.8025	0.8259	0.8264	0.8277	0.8393	0.8313	0.8347
Leaves	×2	PSNR	27.4519	28.8226	28.9736	29.0358	31.1967	29.3018	29.5426
		SSIM	0.9251	0.9363	0.9374	0.9389	0.9493	0.9402	0.9420
Parrots	×2	PSNR	31.3765	32.6828	32.7066	32.7360	33.5052	32.9107	33.0060
		SSIM	0.9280	0.9346	0.9348	0.9355	0.9416	0.9386	0.9382
Raccoon	×2	PSNR	30.9388	31.9138	32.0159	32.0788	32.4398	32.1853	32.2964
		SSIM	0.8439	0.8800	0.8849	0.8865	0.8966	0.8890	0.8921
Starfish	×2	PSNR	30.2341	31.4485	31.4869	31.5531	32.4093	31.7055	31.8238
		SSIM	0.8896	0.9113	0.9121	0.9136	0.9233	0.9147	0.9168
Average	×2	PSNR	30.0768	31.1889	31.2590	31.3072	32.2869	31.4576	31.5708
		SSIM	0.8725	0.8915	0.8926	0.8935	0.9041	0.8967	0.8980

Fig. 3. Comparison of SR results on Plants by different methods (scaling factor $s = 3$), from left to right and from top to bottom: Bicubic, ScSR[13], ANR[17], ASCSR[33], SRCNN[26], ASR+LR[34], Proposed method.

Fig. 4. Comparison of SR results on Butterfly by different methods (scaling factor $s = 3$), from left to right and from top to bottom: Bicubic, ScSR[13], ANR[17], ASCSR[33], SRCNN[26],ASR+LR[34], Proposed method.

Table 2. Comparison of our method with Bicubic, ScSR[13], ANR[17], ASCSR[33], SRCNN[26] and ASR+LR[34](scaling factor $s = 3$).

Image		Criterion	Bicubic	ScSR	ANR	ASCSR	SRCNN	ASR+LR	Ours
Plants	×3	PSNR	31.0944	31.3387	31.5526	31.6871	32.4816	31.7753	31.8659
		SSIM	0.8340	0.8428	0.8474	0.8488	0.8669	0.8503	0.8547
Bike	×3	PSNR	22.8135	23.3357	23.4027	23.4263	24.4864	23.3169	23.4574
		SSIM	0.6830	0.7136	0.7228	0.7249	0.7427	0.7234	0.7269
Butterfly	×3	PSNR	24.0558	24.7012	24.8138	24.8771	26.5799	24.8528	24.9449
		SSIM	0.8264	0.8316	0.8322	0.8328	0.8595	0.8325	0.8337
Flower	×3	PSNR	27.4608	27.7456	27.9469	27.9531	28.9981	28.1433	28.2447
		SSIM	0.7705	0.7827	0.7931	0.7933	0.8111	0.8002	0.7997
Girl	×3	PSNR	32.7046	32.5367	32.9312	33.0901	33.6761	33.2411	33.1840
		SSIM	0.6905	0.7022	0.7084	0.7113	0.7176	0.7150	0.7143
Parthenon	×3	PSNR	26.0415	26.0518	26.2983	26.3692	26.9895	26.4212	26.5532
		SSIM	0.6865	0.6954	0.7021	0.7038	0.7144	0.7092	0.7112
Leaves	×3	PSNR	23.4596	24.1175	24.2977	24.3847	25.4772	24.3026	24.4624
		SSIM	0.8002	0.8304	0.8329	0.8356	0.8604	0.8337	0.8395
Parrots	×3	PSNR	28.0973	28.7211	28.8623	28.9341	29.7291	28.9784	29.0563
		SSIM	0.8716	0.8699	0.8744	0.8778	0.8873	0.8827	0.8833
Raccoon	×3	PSNR	28.3971	28.3827	28.5666	28.6794	29.0984	28.7547	28.8693
		SSIM	0.7065	0.7214	0.7358	0.7373	0.7470	0.7438	0.7447
Starfish	×3	PSNR	27.0022	27.1137	27.3744	27.4052	28.4517	27.6890	27.7772
		SSIM	0.7834	0.7895	0.7955	0.7991	0.8215	0.8122	0.8173
Average	×3	PSNR	27.1127	27.4045	27.6047	27.6804	28.5968	27.7475	27.8415
		SSIM	0.7653	0.7780	0.7845	0.7865	0.8028	0.7903	0.7925

4.2 Discussion about the Parameter Settings in Our Method

The low-rank property of our method means that objective function (6) drops the edge-preserving regularization term $\|E \otimes \alpha\|_2^2$ when $\lambda_2 = 0$. Then the objective function is equivalent to the ASCSR model proposed in [33], the low-rank property and corresponding parameter settings have already been discussed in [33] and we don't repeat here. Extracting the gradient domain guided filter of every HR dictionary atom, the high-frequency details in the HR dictionary can be utilized as the prior information. In this subsection, we mainly discuss the settings of the trade-off parameter λ_2. In **Fig. 5**, when λ_2 is changed from 0 to 0.5, the PSNR and SSIM average curves of ten test images obtained by our proposed

method are plotted, respectively. As a result, when $\lambda_1 = 0.2$ and $\lambda_2 = 0.01$, both of them reach the peak. And after $\lambda_2 = 0.2$, PSNR and SSIM tend to stable.

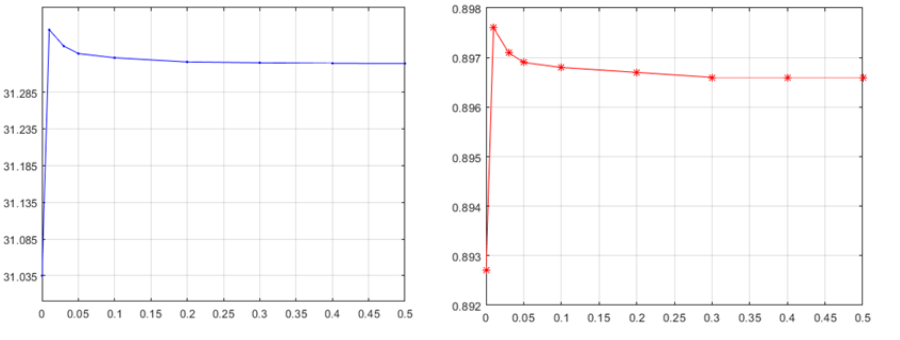

Fig. 5. From left to right, average effect of PSNR and SSIM values on different λ_2.

4.3 Robustness of Our Proposed Method

In practice, the images are usually contaminated by noises. Herein, we choose any six of the ten test images, which are Bike, Butterfly, Leaves, Parrots, Raccoon and Starfish to evaluate the robustness of our method against noise. Gaussian noises with a standard deviation of $2,4,6$ are respectively chosen to add into the input LR images, corresponding to λ_1=0.2, 0.4, 0.6; and λ_2 is a constant $\lambda_2 = 0.1$. **Table 3** lists the average PSNR and SSIM values for the six reconstructed images obtained through different methods under different Gaussian noises. Although the performance of SRCNN is the best among the above algorithms, our proposed algorithm achieves the best objective results among the sparse representation-based approaches. Furthermore, in order to get better reconstruction results, SRCNN requires higher overhead during training, such as a large number of samples, more model parameters, and a lot of time. **Fig. 6** and **7** illustrate the visual effect of Bike and Starfish. As we know, noises degrade the image quality. From results, the proposed method and the ASR+LR have higher performance than other methods since they may well in suppressing noises. That is the low-rank constraint helps to enhance image SR robustness.

Fig. 6. SR results on Bike by different methods (scaling factor $s = 2, \sigma = 6$), from left to right and from top to bottom: Bicubic, ScSR[13], ANR[17], ASCSR[33], SRCNN[26], ASR+LR[34], Proposed method.

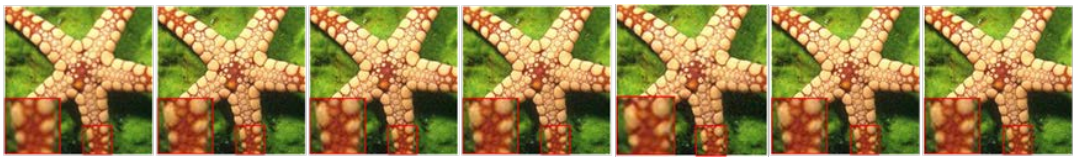

Fig. 7. SR results on Starfish by different methods (scaling factor $s = 3, \sigma = 6$), from left to right and from top to bottom: Bicubic, ScSR[13], ANR[17], ASCSR[33], SRCNN[26], ASR+LR[34], Proposed method.

Table 3. Average PSNR (dB) and SSIM results on noisy images (Bike, Butterfly, Leaves, Parrots, Raccoon, Starfish).

Noise Level	Criterion	Bicubic	ScSR	ANR	ASCSR	SRCNN	ASR+LR	Ours
0	PSNR	28.8548	30.1218	30.2095	30.2515	31.4302	30.4539	30.5586
	SSIM	0.8901	0.9090	0.9105	0.9116	0.9233	0.9144	0.9157
2	PSNR	28.8058	29.9393	30.0566	30.1588	31.2903	30.2721	30.3711
	SSIM	0.8809	0.8935	0.8954	0.8979	0.9020	0.8996	0.9006
4	PSNR	28.6626	29.4496	29.5682	29.6457	30.6288	29.7613	29.8531
	SSIM	0.8569	0.8571	0.8597	0.8612	0.8774	0.8632	0.8644
6	PSNR	28.4390	28.7579	28.8619	28.9579	29.7100	29.0648	29.1251
	SSIM	0.8233	0.8097	0.8213	0.8236	0.8362	0.8259	0.8271

4.4 Discussion on the Performance of Noisy Real Word Image

Actual noisy images in SUN database [45] are used to verify our method in this section. Two actual images (as shown in **Fig. 8**) are selected, and the regions of interest (ROI) marked in the figures are reconstructed to verify the feasibility and robustness of the approach in practice. We perform SR reconstruction on the ROI areas in Airport and Building with the magnification factor 3. **Fig. 9** and **10** display the visual comparison of SR results obtained by our method with Bicubic, ScSR, ANR, ASCSR, SRCNN and ASR+LR. As shown in the two figures, we get the following conclusion. Firstly, the Bicubic produces the most blurred image. Then, ASCSR and ASR+LR generate better results than ScSR and ANR, since the edges of the image are cleaner. Finally, our proposed method well preserves the edges and reveals more robust against noise than other sparse representation-based methods. Compared to SRCNN, our method almost has the similar visual effect as it does. The experimental results indicate that our method can be applied to real word noisy images and meet the need of actual image reconstruction.

Fig. 8. From left to right, actual noisy images: Airport, Building and their corresponding ROI areas for testing.

Fig. 9. SR results of the ROI in Airport image by different methods (scaling factor $s = 3$), from left to right and from top to bottom: Bicubic, ScSR[13], ANR[17], ASCSR[33], SRCNN[26] , ASR+LR[34], Proposed method.

Fig. 10. SR results of the ROI in Building image by different methods (scaling factor $s = 3$), from left to right and from top to bottom: Bicubic, ScSR[13], ANR[17], ASCSR[33], SRCNN[26] , ASR+LR[34], Proposed method.

5. Conclusion

In this paper, the gradient domain guided filter of HR dictionary atoms is introduced into the LRR scheme as an edge-preserving regularization term, and a robust SISR reconstruction method is proposed. Through experimental results, the LRR is proved to effectively capture the global structure of the image. The gradient domain guided filter incorporates an explicit first-order edge-aware constraint to enhance the fine detail of an image based on local optimization. The proposed method integrates the edge-preserving regularization term into the LRR, which can simultaneously exploit both the global and local structure of the image to ensure the quality of the restored HR image. Extensive experiments on test images demonstrate that the proposed approach is more competitive than some other state-of-the-art methods.

Acknowledgments

This work is supported by the National Natural Science Foundation of China under grant No. 51774281 and National Key Research and Development Project of China under grant No. 2018YFC0808302.

References

[1] Y. Zhang, Q. Fan, F. Bao, Y. Liu, and C. Zhang, “Single-image super-resolution based on rational fractal interpolation,” *IEEE Transactions on Image Processing*, vol. 27, no. 8, pp. 3782-3797, Aug. 2018. Article (CrossRef Link)

[2] X. Li and M.T. Orchard, “New edge-directed interpolation,” *IEEE Transactions on Image Processing*, vol. 10, no. 10, pp. 1521-1527, Oct. 2001. Article (CrossRef Link)

[3] F. Shi, J. Cheng, L. Wang, P-T. Yap, and D.G. Shen, “LRTV: MR image super-resolution with low-rank and total variation regularizations,” *IEEE Transactions on Medical Imaging*, vol. 34, no. 12, pp. 2459-2466, Dec. 2015. Article (CrossRef Link)

[4] K. Chang, P. L. K. Ding, and B. Li, "Single image super-resolution using collaborative representation and non-local self-similarity," *Signal Processing*, vol. 149, pp. 49-61, Feb. 2018. Article (CrossRef Link)
[5] K. Zhang, X. Gao, J. Li, and H. Xia, "Single image super-resolution using regularization of non-local steering kernel regression," *Signal Processing*, vol. 123, pp. 53-63, Nov. 2016. Article (CrossRef Link)
[6] K. Zhang, X. Gao, D. Tao, and X. Li, "Single image super-resolution with non-local means and steering kernel regression," *IEEE Transactions on Image Processing*, vol. 21, no.11, pp. 4544-4556, Nov. 2012. Article (CrossRef Link)
[7] S. Dai, M. Han, W. Xu, Y. Wu, Y. Gong, and A. K. Katsaggelos, "SoftCuts: a soft edge smoothness prior for color image super-resolution," *IEEE Transactions on Image Processing*, vol. 18, no. 5, pp. 969-981, May. 2009. Article (CrossRef Link)
[8] Y-W. Tai, S. Liu, M. S. Brown, and S. Lin, "Super resolution using edge prior and single image detail synthesis," in *Proc. of IEEE Conf. on Computer Vision and Pattern Recognition*, pp. 2400-2407, 2010. Article (CrossRef Link)
[9] J. Sun, Z. Xu, and H-Y. Shum, "Gradient profile prior and its applications in image super-resolution and enhancement," *IEEE Transactions on Image Processing*, vol. 20, no. 6, pp. 1529-1542, Jun. 2011. Article (CrossRef Link)
[10] Q. Yan, Y. Xu, X. Yang, and T. Q. Nguyen, "Single image super-resolution based on gradient profile sharpness," *IEEE Transactions on Image Processing*, vol. 24, no. 10, pp. 3187-3202, Oct. 2015.
[11] H. Chen, X. He, Q. Teng and C. Ren, "Single image super resolution using local smoothness and nonlocal self-similarity priors," *Signal Processing: Image Communication*, vol. 43, pp. 68–81, Jan. 2016. Article (CrossRef Link)
[12] J. Yang, J. Wright, T. Huang, and Y. Ma, "Image super-resolution as sparse representation of raw image patches," in *Proc. of IEEE Conf. on Computer Vision and Pattern Recognition*, pp. 1-8, Jun. 2008. Article (CrossRef Link)
[13] J. Yang, J. Wright, T. Huang, and Y. Ma, "Image super-resolution via sparse representation," *IEEE Transactions on Image Processing*, vol. 19, no. 11, pp. 2861-2873, Nov. 2010. Article (CrossRef Link)
[14] H. Chang, D-Y. Yeung, and Y. Xiong, "Super-resolution through neighbor embedding," in *Proc. of IEEE Conf. on Computer Vision and Pattern Recognition*, pp. 275-282, Jul. 2004. Article (CrossRef Link)
[15] W. Dong, L. Zhang, G. Shi, and X. Wu, "Image deblurring and super-resolution by adaptive sparse domain selection and adaptive regularization," *IEEE Transactions on Image Processing*, vol. 20, no. 7, pp. 1838-1857, Jul. 2011. Article (CrossRef Link)
[16] Y. Tang, W. Gong, Q. Yi, and W. Li, "Combining sparse coding with structured output regression machine for single image super-resolution," *Information Science*, vol. 430-431, pp. 577-598, 2018. Article (CrossRef Link)
[17] R. Timofte, V. D. Smet, and L. V. Gool, "Anchored neighborhood regression for fast example-based super-resolution," in *Proc. of IEEE International Conf. on Computer Vision*, pp. 1920-1927, Dec. 2013. Article (CrossRef Link)
[18] R. Timofte, V. D. Smet, and L. V. Gool, "A+: Adjusted anchored neighborhood regression for fast super-resolution." in *Proc. of Asian Conf. on Computer Vision*, pp. 111-126, 2014. Article (CrossRef Link)
[19] C. Zhang, W. Liu, J. Liu, C. Liu, and C. Shi, "Sparse representation and adaptive mixed samples regression for single image super-resolution," *Signal Processing: Image Communication*, vol. 67, pp. 79-89, 2018. Article (CrossRef Link)
[20] D. Cheng, L. Chen, Y. Cai, L. You, and Y. Tu, "Image super-resolution reconstruction based on multi-dictionary and edge fusion," *Journal of China Coal Society*, vol. 43, no. 7, pp. 2084－2090, Jul. 2018. Article (CrossRef Link)

[21] C. Ren, X. He, and T.Q. Nguyen, "Single image super-resolution via adaptive high-dimensional non-local total variation and adaptive geometric feature," *IEEE Transactions on Image Processing*, vol. 26, no. 1, pp. 90-106, Jan. 2017. Article (CrossRef Link)
[22] B. Li, H. Chang, S. Shan, and X. Chen, "Locality preserving constraints for super-resolution with neighbor embedding," in *Proc. of IEEE International Conf. on Image Processing*, pp. 1189-1192, 2009. Article (CrossRef Link)
[23] K. Zhang, X. Gao, X. Li, and D. Tao, "Partially supervised neighbor embedding for example-based image super-resolution," *IEEE Journal Selected Topics Signal Processing*, vol. 5, no. 2, pp. 230-239, Apr. 2011. Article (CrossRef Link)
[24] X. Gao, K. Zhang, D. Tao, and X. Li, "Image super-resolution with sparse neighbor embedding," *IEEE Transactions on Image Processing*, vol. 21, no. 7, pp. 3194-3205, Jul. 2012. Article (CrossRef Link)
[25] J. Jiang, X. Ma, C. Chen, T. Lu, Z. Wang, and J. Ma, "Single image super-resolution via locally regularized anchored neighborhood regression and nonlocal means," *IEEE Transactions on Multimedia*, vol. 19, no. 1, pp. 15-26, Jan. 2017. Article (CrossRef Link)
[26] C. Dong, C. C. Loy, K. He, and X. Tang, "Image super-resolution using deep convolutional networks," *IEEE Transactions on Pattern Analysis & Machine Intelligence*, vol. 38, no. 2, pp. 295-307, Feb. 2016. Article (CrossRef Link)
[27] K. Zeng, Jun Yu, R. Wang, C. Li, and D. Tao, "Coupled deep autoencoder for single image super-resolution," *IEEE Transactions on Cybernetics*, vol. 47, no. 1, pp. 27-37, Jan. 2017. Article (CrossRef Link)
[28] L. Chen, Q. Kou, D. Cheng, and J. Yao, "Content-guided deep residual network for single image super-resolution," *Optik*, vol. 202, Feb, 2020. Article (CrossRef Link)
[29] R. Zeyde, M. Elad, and M. Protter, "On single image scale-up using sparse-representations," in *Proc. of 7th International Conf. on Curves Surfaces*, pp. 711-730, 2010. Article (CrossRef Link)
[30] S. Huang, J. Sun, Y. Yang, Y. Fang, and P. Lin "Robust single-image super-resolution based on adaptive edge-preserving smoothing regularization," *IEEE Transactions on Image Processing*, vol. 27, no. 6, pp. 2650-2663, Jun. 2018. Article (CrossRef Link)
[31] F. Kou, W. Chen, C. Wen, and Z. Li, "Gradient domain guided image filtering," *IEEE Transactions on Image Processing*, vol. 24, no. 11, pp. 4528-4539, Nov. 2015. Article (CrossRef Link)
[32] X. Chen and C. Qi, "Low-rank neighbor embedding for single image super-resolution," *IEEE Signal Processing Letters*, vol. 21, no. 1, pp. 79-82, Jan. 2014. Article (CrossRef Link)
[33] J. Zhao, H. Hu, and F. Cao, "Image super-resolution via adaptive sparse representation," *Knowledge-Based-Systems*, vol. 124, pp. 23-33, 2017. Article (CrossRef Link)
[34] X. Li, G. Gao, Y. Zhang, and B. Wang, "Single image super-resolution via adaptive sparse representation and low-rank constraint," *Journal of Visual Communication & Image Representation*, vol. 55, pp. 319-330, 2018. Article (CrossRef Link)
[35] T. Lu, Z. Xiong, Y. Zhang, B. Wang, and T. Lu, "Robust face super-resolution via locality-constrained low-rank representation," *IEEE Access*, 5, pp. 13103-13117, 2017. Article (CrossRef Link)
[36] W. Dong, G. Shi, X. Li, Y. Ma, and F. Huang, "Compressive sensing via nonlocal low-rank regularization," *IEEE Transactions on Image Processing*, vol. 23, no. 8, pp. 3618-3632, Aug. 2014. Article (CrossRef Link)
[37] W. Gong, Q. Li, Y. Tang, and W. Li, "Multi-layer strategy and reconstruction model with low rank and local rank regularizations for single image super-resolution," *Signal Processing: Image Communication*, vol. 57, 197–210, 2017. Article (CrossRef Link)
[38] N. Han, Z. Song, and Y. Li, "Cluster-based image super-resolution via jointly low-rank and sparse representation," *Journal of Visual Communication & Image Representation*, vol. 38, pp. 175-185, 2016. Article (CrossRef Link)
[39] J.Shi and C.Qi, "Low-rank representation for single image super-resolution via self-similarity learning," in *Proc. of IEEE International Conf. on Image Processing*, pp. 1424-1428, 2016. Article (CrossRef Link)

[40] G. Liu, Z. Lin, S. Yan, J. Sun, Y. Yu, and Y. Ma, "Robust recovery of subspace structures by low-rank representation," *IEEE Transactions on Pattern Analysis & Machine Intelligence*, vol. 35, no. 1, pp. 171-184, Jan. 2013. Article (CrossRef Link)
[41] K. Tang, R. Liu, Z. Su, and J. Zhang, "Structure-constrained low-rank representation," *IEEE Transactions on Neural Networks & Learning System*, vol. 25, no. 12, pp. 2167-2179, Dec. 2014. Article (CrossRef Link)
[42] J. Wen, B. Zhang, Y. Xu, J. Yang, and N. Han, "Adaptive weighted nonnegtive low-rank representation," *Pattern Recognition*, vol. 81, pp. 326-340, 2018. Article (CrossRef Link)
[43] S. Boyd, N. Parikh, E. Chu, B. Peleato, and J. Eckstein, "Distributed optimization and statistical learning via the alternating direction method of multipliers," *Foundations and Trends in Machine Learning*, vol. 3, no. 1, pp. 1-122, 2011. Article (CrossRef Link)
[44] E. Grave, G. Obozinski, and F. Bach, "Trace lasso: a trace norm regularization for correlated designs," in *Proc. of Advances in Neural Information Processing Systems*, pp. 2187-2195, 2011. Article (CrossRef Link)
[45] J. Xiao, J. Hays, K. A. Ehinger, and A. Torralba, "Sun database: large-scale scene recognition from abbey to zoo," in *Proc. of IEEE Conf. on Computer Vision and Pattern Recognition*, pp. 3485-3492, 2010. Article (CrossRef Link)

Rui Gao received the B.S. degree in Mathematics and Applied Mathematics in 2003 from the School of Mathematics and Statistics, Xinyang Normal University. She received the M.S. degree in Applied Mathematics in 2006 from the School of Science, Northwestern Polytechnical University. She is currently pursuing the Ph.D. degree in the School of Information and Control Engineering, China University of Mining and Technology. Her research interests include image processing, image super-resolution and machine learning.

Deqiang Cheng received the B.S., M.S. and Ph.D. degrees in Electrical and Information Engineering from China University of Mining and Technology. He is now a Professor at China University of Mining and Technology. His research interests include machine learning, video coding, image processing and pattern recognition.

Jie Yao received the M.S. degree in detection technology and automation equipment from China University of Mining and Technology in 2013, where she is currently pursuing the Ph.D. degree with the School of Information and Control Engineering, China University of Mining and Technology. Her current research interests include image and video processing, image and video interpolation and super-resolution.

Liangliang Chen received the B.S. degree in electrical and information engineering from the China University of Mining and Technology in 2016, where he is currently pursuing the Ph.D. degree with the School of Information and Control Engineering, China University of Mining and Technology. His general interests lie in image and video processing and pattern recognition.